

# Numerical simulation of wave propagation in 2-D fractured media: scattering attenuation at different stages of the growth of a fracture population

Serafeim Vlastos,<sup>1,2,\*</sup> Enru Liu,<sup>1,†</sup> Ian G. Main<sup>2</sup> and Clement Narteau<sup>2,3</sup>

<sup>1</sup>British Geological Survey, Murchison House, West Mains Road, Edinburgh EH9 3LA, UK

<sup>2</sup>School of GeoSciences, University of Edinburgh, West Mains Road, Edinburgh EH9 3JW, UK

<sup>3</sup>Laboratoire de Dynamique des Systemes Geologiques, Institut de Physique du Globe de Paris, 4 Place Jussieu, 75252 Paris cedex 05, France

Accepted 2007 August 8. Received 2007 August 7; in original form 2006 September 1

## SUMMARY

In this paper, we systematically examine the multiple scattering process of seismic waves at consecutive stages of the evolution of 2-D fracture population. Synthetic seismograms are computed using the pseudo-spectral method for elastic wave propagation, where spatial derivations are computed using fast Fourier transforms and time derivatives are computed using second-order finite differences. The grid sizes are  $2560 \times 2560$  with 1 m interval and a Ricker wavelet with a peak frequency of 30 Hz is used (or equivalently a wavelength of 10 m for the *P*-wave velocity of  $3000 \text{ m s}^{-1}$  used in our modelling). Fracture patterns are generated using a 2-D cellular automaton model of rupture with healing to account for clustering and anisotropy in the fracture growth process. The cellular automation model takes into account the discontinuous and segmented nature of a fracture population, and reproduces in the statistical sense the intermediate stages of fracture growths. To estimate the frequency-dependence of scattering attenuation (quantified by the inverse quality factor  $Q^{-1}$ ) at different stages of the fracture evolution, we use the spectral ratio method. Variations of  $Q^{-1}$  with frequency are then fitted to a polynomial of order up to 8 for each state of the fracture evolution as we do not want to make an assumption about how  $Q^{-1}$  should depend on frequency or scales. This allows us to determine the nature of the frequency-dependence of scattering attenuation as a function of fracture evolution. Our results confirm, as expected, the dependence of scattering attenuation on frequency, and the fifth-order polynomial seems to fit the measured attenuation from synthetic seismograms better. In addition, the inverse quality factor  $Q^{-1}$  is shown to be linearly dependent on fracture density, reaching a maximum when fracture density is the highest. In summary, our numerical results confirm that scattering attenuation has a complex dependence on frequency, and measurements of attenuations may be potentially used to characterize spatial distributions of fracture networks in particular, the scale distributions.

**Key words:** attenuation, cellular automaton, fractures, multiscattering, seismic wave propagation.

## 1 INTRODUCTION

Rock mechanical and hydraulic properties are greatly affected by the existence of fractures. Most fractures propagate not only as the result of the purely mechanical effects of an ambient stress field, but also due to the effect of a stress concentration at the crack tips.

Seismic waves can be an effective tool for locating fractures and characterizing their properties because of the sensitivity of wave velocities, amplitudes and spectral characteristics to fracture compliance. These effects are known to be time-dependent (e.g. Jin & Aki 1986), a phenomenon more likely to result from changes in fracture geometry or fluid content than changes in other permanent types of geological heterogeneities. This holds out the possibility of distinguishing the relative contribution of either in a real case. The effects of aligned fluid-filled microcracks on velocity anisotropy (including shear wave splitting) and scattering attenuation have been considered in the long wavelength limit for low crack densities by Hudson (1981, 1986) and Crampin (1978, 1984), using a single

\*Now at: Papaflessa 29, GR 15125 Marousi, Athens, Greece.

†Now at: ExxonMobil Upstream Research Co., P.O. Box 2189, Houston, TX 77252-2189, USA. E-mails: eliu0103@hotmail.com; Enru.Liu@exxonmobil.com

scattering approximation and including viscous losses. These studies show that the theory (which is second order in velocities but first order in attenuation) is adequate for interpretation of the velocity anisotropy, but has so far been unable to reproduce either the observed magnitude or the frequency dependence of quality factor ( $Q$ ) found in the earth's crust (Main *et al.* 1990). This may be because intrinsic attenuation associated with fluids has wrongly been attributed to scattering or because the theories are often applied to sparse arrays of smooth, elliptical, discrete microcracks of identical size, shape (aspect ratio) and orientation in a homogeneous medium. Though scattering from cracks is usually weak and can be negligible according to first-order (in crack density) theory as shown by Main *et al.* (1990) and Peacock & Hudson (1990), Pointer *et al.* (2000), Chapman (2003), Yang *et al.* (2007) and Yang & Zhang (2002) have shown that, if allowance is made for fluid flow between cracks, first-order theory predicts attenuation levels in line with observations.

When we examine the properties and the behaviour of a fractured network, it is very important to create a network that may represent the properties of fractures in natural rocks. We use a model of rupture designed to reproduce structural patterns observed in the formation and evolution of a population of strike-slip faults and fractures (Narteau 2007). This model is a multiscale cellular automaton with two states. An active state represents actively slipping fracture segments. A stable state represents 'intact' zones in which the fracturing process is confined to a smaller scale. At the elementary scale, the transition rates from one state to another are determined with respect to the magnitude of the local strain rate and a time-dependent stochastic process. At increasingly larger scales, healing and fracturing are described according to geometric rules of interaction between active fault segments based on fracture mechanics. A redistribution of the strain rates in the neighbourhood of active faults at all scales ensures long range interactions and non-linear feedback processes are incorporated in the fracture growth mechanism. Typical patterns of development of a population of faults are presented here involving nucleation, growth, branching, interaction and coalescence. The initial material properties are uniform, so the complex behaviours result solely from the competition between random fluctuations and deterministic physical interactions. Consequently, the entire process of fault development is an emergent property of the model of fault interaction and does not depend on pre-existing material heterogeneity.

In this paper, we model seismic wave propagation in each of the consecutive stages of evolution of the fracture network. We use a pseudo-spectral technique where fractures with a vanishing width are implemented using an effective medium theory (following Coates & Schoenberg 1995; Vlastos *et al.* 2003, 2006). Fractures are represented using the displacement discontinuity model of Schoenberg (1980), Pyrak-Nolte *et al.* (1990a) and Liu *et al.* (2000). We show wavefield snapshots at a certain time step for each stage of the fracture evolution and demonstrate that the evolving fracture network can be systematically related with wavefield characteristics, for example, scattering quality factor  $Q^{-1}$ . We calculate attenuation as a function of frequency for each stage and fit the results with a polynomial, and then use a parsimonious statistical method to pick the best-fitting polynomial consistent with the data. Finally, we present seismic traces at two source–receiver directions, that is, parallel and perpendicular to the fracture orientation, to see the azimuthal dependence of scattering. Our results show that there is a significant frequency dependence of scattering attenuation, and high values of attenuation observed at certain frequencies may be linked to characteristic scales of heterogeneities. Also fracture density varies systematically as the network evolves, results in signif-

icant changes in attenuation. In addition, our results exhibit that scattering is also influenced by the angle between the direction of propagation and the orientation of the fractures (implying scattering related attenuation anisotropy). Note that in real fractured rock, it is very likely that both fluid-related intrinsic absorptions and fracture-related scattering attenuation will affect wavefields. Separations of their effects remain a popular subject and in this paper we only consider scattering attenuation and have not considered the effects of fluids in fractures.

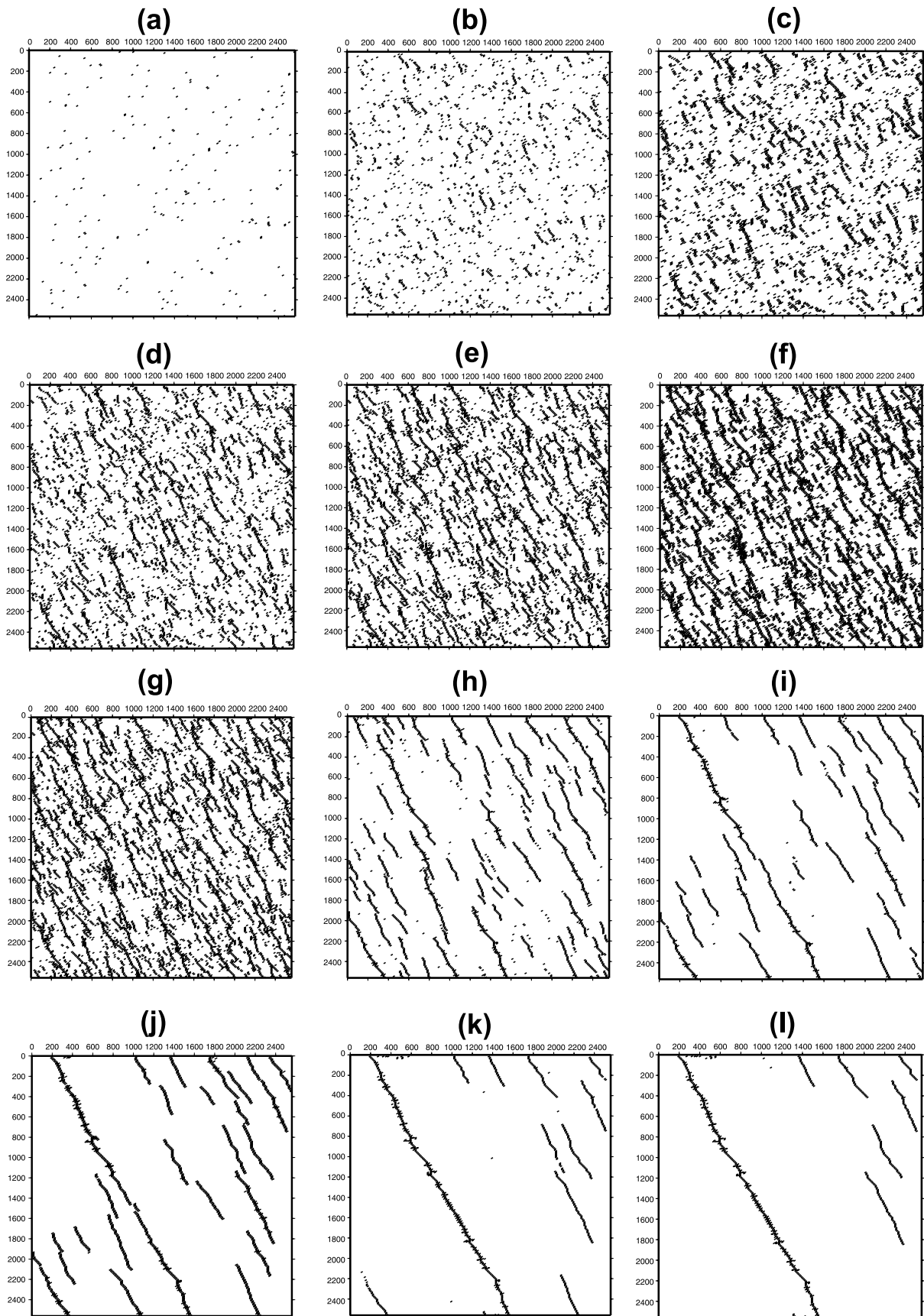
## 2 MODEL FRACTURE NETWORKS

Over the last 10 yr, the geostatistical modelling of fracture populations has become a well-established approach with a large variety of applications as reviewed by Bonnet *et al.* (2001). Here we use instead a combined stochastic/physical model of rupture with healing to generate fracture patterns at different stages of the development of a population of strike-slip fractures. This model is a cellular automaton with long range interaction that has been described by Narteau (2007) in detail, and we only give a brief summary below (see Appendix A for more details).

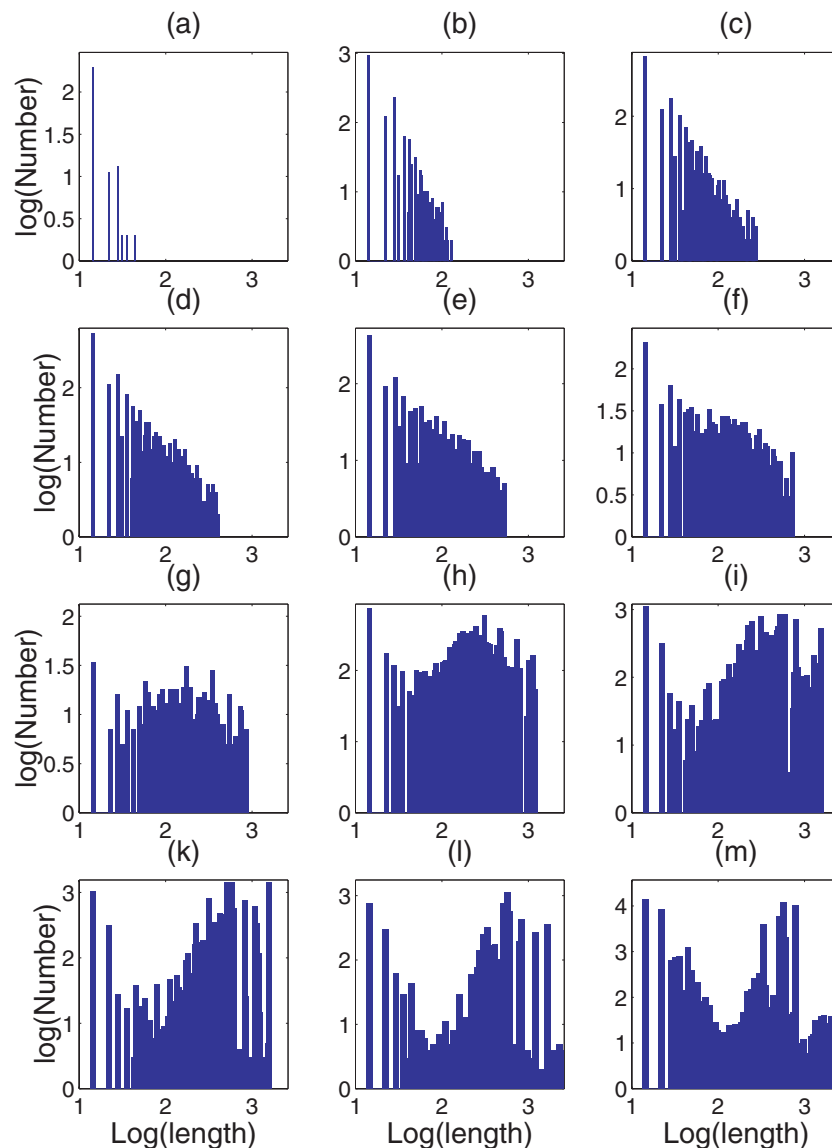
In Narteau's (2007) rupture model, a 2-D regular, uniform square lattice represents a rock mass subject to a constant external tectonic loading. Each cell can be in two states of fracturing (i.e. an active and a stable state) and a local variable represents the local strain rate. The external strain rate is fixed. The whole system is polarized by the orientation of the tectonic loading and the directions of the principal stresses:  $\sigma_1$ ,  $\sigma_2$  and  $\sigma_3$ .  $\sigma_2$  is assumed to be vertical,  $\sigma_1$  and  $\sigma_3$  are oriented following the principal axis of our lattice, and, with respect to the Coulomb–Mohr's theory of fault orientation, only vertical strike-slip fracture segments can form. The loading here favours right-lateral fractures and new segments grow following a main direction, at an angle  $\theta$  from the maximum compressive stress. The angle ( $\theta$ ) here is taken to be approximately to  $30^\circ$  implying a conventional coefficient of the internal friction  $\mu \approx 0.6$ .

Fig. 1 is an example of fracture evolution models from Narteau (2007). Starting with a spatially uniform 'intact' model, an element is selected at random to fail, thereby increasing the strain rate there, and changing the strain rate around itself by an amount proportional to the change in Coulomb stress. In this sense the rules of fracture mechanics for a soft inclusion (changes in normal and shear stress, accelerated deformation due to stress concentration at the crack tip) are combined with a frictional process that determines a finite slip rate on the fault, and a reduction in deformation rate in the stress shadows around the fault. Since this is a cellular automaton, these rules are not implemented exactly, merely in how a broken element rearranges the local deformation rate. However, the model is conditioned on exact known solutions for Coulomb stress redistribution that are reproduced for faults of finite length. The next fracture will then occur preferentially at the zones of high stress concentration or high strain rate, but initially it is more common to nucleate a new fracture elsewhere, since small faults affect only their immediate neighbourhood.

Once sufficient nucleation points have been established, the faults then enter a growth phase where the stress concentration at the fault tips becomes the dominant effect, and the slip rate tends to increase in the centre of mature faults due to strong feedback (mutual amplification of strain rate) between elements aligned at  $30^\circ$  to  $\sigma_1$ . At this stage the strain rate is changed in a spatial domain that grows with fault length using a multiscale rule where the elementary size is changed from 1 to 2 to 3 units, etc., up to the largest scale and



**Figure 1.** Fracture patterns that represent consecutive stages at the evolution of the fracturing. The horizontal direction is the  $x$ -direction (m) and the vertical direction is the  $y$ -direction (m).



**Figure 2.** Frequency–length distributions of fractures in log–log plots corresponding to fracture distributions in Fig. 1.

then in an inverse cascade back to the smallest. This preserves the cellular automaton rule of nearest neighbour interactions, which (in a coarse-grained way) including long-range interactions needed to produce the required degree of spatial self-organization of natural fault populations.

In a third stage the faults begin to interact, either coalescing to form larger ones, or switching off if they are in the stress shadow of a larger fault, and are more likely to heal than to nucleate. The healing rate is assumed constant and spatially uniform. The ratio of the loading and healing rates determine the overall geometries of the fault population at steady state. However, here we use a single run at a constant value of both, and instead look at snapshots of the temporal evolution where we start with a dilute, distributed fracture population, and end with a single megafault with an infinite correlation length. In response to tectonic loading, this permanent internal process of evolution between the local strain rates and a population of fault segments may be described as a ‘self-organized’ process (Sornette *et al.* 1994) the order and structures emerge spontaneously rather than being prescribed *a priori* as in a geostatistical

model (which can be seen more clearly in Fig. 2, where frequency–length distribution in log–log scale is given for each of the eight models in Fig. 1). It is important to emphasize here that we use this model only as a device to produce realistic-looking fracture patterns with varying fracture density, power-law size and spacing distributions, and correlation length, in the absence of geostatistical models that reproduce the first three, but not the last.

### 3 NUMERICAL SIMULATION OF WAVE PROPAGATION

The effect of fracture properties on wave behaviour can be described quantitatively by modelling a fracture as a non-welded interface with a vanishing thickness described by a simple constitutive model referred to in the literature as linear slip or displacement–discontinuity boundary conditions (Schoenberg 1980; Pyrak-Nolte *et al.* 1990a,b). The key parameter called fracture stiffness (i.e. the inverse of fracture compliance), can be determined experimentally (Pyrak-Nolte *et al.* 1990a,b). More realistic fracture models consisting of a

distribution of small cracks (voids) or contacts along a plane have been given by (Liu *et al.* 1995; Hudson *et al.* 1996, 1997) and reviewed by Liu *et al.* (2000).

We conduct 2-D forward modelling for each one of the models that represent stages (a)–(k) (Fig. 1) of the fracture network evolution, to examine the variation in scattering attenuation and investigate its frequency dependence. To ensure consistency between the different models we use the same background medium in all the cases. The background medium parameters are  $P$ - and  $S$ -wave velocities of  $V_P = 3300 \text{ m s}^{-1}$ ,  $V_S = 2000 \text{ m s}^{-1}$ , and a mass density of  $\rho = 2200 \text{ kg m}^{-3}$ . In this study, we assume that the normal ( $Z_N$ ) and tangential ( $Z_T$ ) fracture compliances are constant with  $Z_T = Z_N = 5.6 \times 10^{-11} \text{ Pa}^{-1}$ . Note that we expect that fracture compliance will depend on fracture scaling and frequency as shown by Barton & Bandis (1980); Pyrak-Nolte & Nolte (1992). More recently there is a renewed interest of fracture/scale-dependence of fracture compliance, see Liu *et al.* (2001), Liu (2005), Lubbe & Worthington (2006), Liu *et al.* (2007) and Yue *et al.* (2007). Nevertheless the assumption of the equivalence of normal and tangential fracture compliance is not unrealistic for most geophysical applications (Barton 2007). Barton (2007) in his recent book discussed in great details of geophysical and geomechanical applications of fracture compliances. The study of frequency/scale dependence of fracture compliance as studied in Liu *et al.* (2006) is beyond the scope of this paper.

We use  $2560 \times 2560$  finite difference grids with spatial grid interval of 1 m and time step 0.001 s. The source wavelet is a Ricker wavelet with a dominant frequency of 30 Hz and a pulse initial time of 0.1 s (or equivalently the wavelength of 10 m for the velocity of  $3300 \text{ m s}^{-1}$  as used in our modelling). The source is located in the centre of the models ( $x = 1280 \text{ m}$  and  $z = 1280 \text{ m}$ ). Figs 3(a)–(l) shows snapshots of the wavefield taken at 350 ms after the initialization of the source, for the consecutive stages of the evolution of the fracture network shown in Figs 1(a)–(l). At the beginning of the nucleation [stage (a)], there are a few active cells which are smaller than the wavelength and act as individual scatterers, so the wave travels undisrupted with a circular wave front. At stages (b)–(d) the first fractures are created and also interaction and formation of large fractures happens. As a result some fractures act as individual scatterers and others that are larger than the wavelength act as reflectors. In addition, as fracture density increases, multiple scattering attenuation and anisotropy (directional variations) also increase, resulting in the reduction of coherent  $P$ - and  $S$ -wave energy and wave fronts become elliptical. Significant seismic anisotropy is an emergent property of the model in the post-nucleation stage. Note that the elliptical elongation is parallel to the  $y$ -direction and not parallel to the strike of the faults. This is because of the tendency for enechelon connection to occur neighbouring elements to form local clusters in this direction to achieve an average  $30^\circ$  angle specified by the coefficient of friction, that is, each fracture segment is along the  $y$ -direction while the overall fractures which are made of many such small segments along the  $y$ -direction have an average direction of  $30^\circ$  angle from the  $y$ -axis. Stage (e) is close to the percolation threshold, and stage (f) has the highest fracture density. While at stage (g) the deformation begins to localize. All those three stages (e, f and g) have high anisotropy and high multiple scattering, with the maximum occurring at stage (f). In the remaining stages, the number of fractures continues to decrease and long fractures begin to form as deformation localizes further. Multiple scattering attenuation decreases and the same happens with anisotropy. The wave fronts become circular, but because fractures are much longer than the wavelength, they act primarily as long and single reflectors.

## 4 SCATTERING ATTENUATION DUE TO DISTRIBUTED FRACTURES

In the models presented here we have not considered mechanisms that cause intrinsic attenuation, so our results are related only to scattering attenuation, which involves no energy loss, but produces a more extended, lower (or enhanced) amplitudes as a result of destructive (or constructive) interferences.

Various results about frequency dependence of attenuation are summarized by Main *et al.* (1990). If seismic wavelengths  $\lambda$  are much greater than typical size  $a$  of scatterers and the number of scatterers is small enough to ignore multiple scattering,  $Q$  is found to be frequency-dependent according to  $Q^{-1} \propto \omega^3$ , where  $\omega$  is an angular frequency ( $\omega = 2\pi f$ ,  $f$  is the frequency). This classic behaviour is known as Rayleigh scattering. Hudson (1981) applied scattering theory to a sparse fracture system and recovered this result (Rayleigh scattering). Hudson (1981, 1986) also presented theories for seismic velocity in a homogeneous cracked medium, which show that velocity depends on the crack density and aspect ratio, as long as the crack radius remains small compared to the seismic wavelength (long wavelength limit,  $ka \ll 1$  where  $k$  is the wavenumber). In contrast, Wu (1982) and Wu & Aki (1985) modelled the observed scattering in the earth for the case of  $ka \approx 1$ . They used smoothly varying heterogeneous distributions of small cracks, and found that the dimension that determines scattering attenuation is the length scale of heterogeneities in crack density and geometry, but not the dimension of an individual crack. Lerche (1985) and Lerche & Petroy (1986) modelled the case of multiple scattering of a dense array of microcracks with a range of sizes. For a Gaussian distribution of microcrack radii they found  $Q^{-1} \propto \omega^3$ , that is, similar to Rayleigh scattering. However, if the power spectrum of heterogeneities follows a power law (with a fractal dimension of  $m$ ), then the frequency dependence of  $Q$  is given by  $Q^{-1} \propto \omega^\gamma$  with  $\gamma = m-1$  (Wu & Aki 1985), which is a power-law frequency dependence. Based on the evidence from the Cajon Pass borehole logs and seismic scattering for a power-law distribution of fractures in crustal rock, Leary (1995) suggested that a power-law frequency dependence of  $Q^{-1} \propto \omega^{0.57}$  is due to a scale-dependence of fracture density. Leary (1995) argued that it is possible that when seismic waves encounter fractures of a given size, energy is scattered and the amount of scattered energy scales as a power of fracture size.

### 4.1 Estimation of scattering attenuation

The estimation of  $Q$  requires a robust method which can handle rapid spatial changes in recorded waveforms. We use the standard spectral-ratio method or SRM (as appears in many text books, such as Aki & Richards 2002), in which  $Q$  is computed from a straightline fit to spectral ratios of received  $[A(\omega)]$  and source  $[A_0(\omega)]$  power spectra. It is assumed that receivers lie along a common ray path from the source and that two power spectra can be linearly related by a simple attenuation operator. Deviations from a linear spectral ratio are treated as noise, and averaging of the spectra is usually required to give stable estimates of attenuation. The amplitude spectrum  $A(\omega)$  of a wave after travelling a distance  $L$  is given by (see Aki & Richards 2002)

$$A(\omega) = A_0 \exp \left[ \frac{\omega L}{2VQ(\omega)} \right], \quad (1)$$

where  $A(\omega)$  is the amplitude spectrum of the source,  $V$  is the wave velocity and  $Q(\omega)$  is the quality factor, which can be obtained

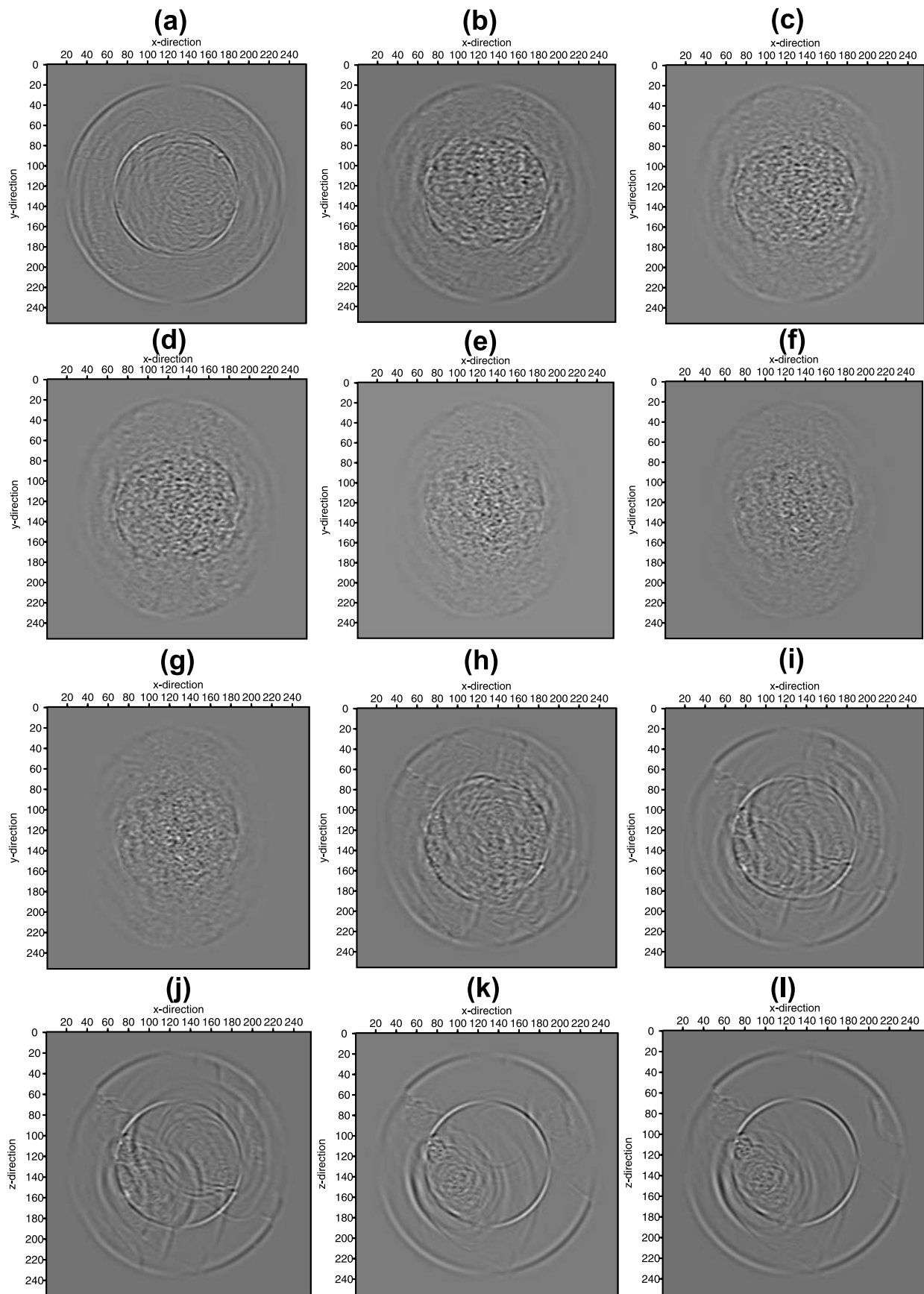


**Figure 3.** Snapshots taken at 350 ms after the initialization of the source. (a)–(i) correspond to the respective fault patterns in Fig. 1. The horizontal direction is the  $x$ -direction ( $\Delta x = 1$  m) and the vertical direction is the  $y$ -direction ( $\Delta y = 1$  m).

by,

$$Q^{-1}(\omega) = \frac{2V}{\omega L} \ln \left[ \frac{A(\omega)}{A_0(\omega)} \right]. \quad (2)$$

Recorded waveforms are first windowed around first  $P$ -wave arrivals, and then Fourier transformed to compute the spectral ratio  $A(\omega)/A_0(\omega)$ . This ratio may in some cases yield negative values, corresponding to a magnification (or enhancement) of input signals caused by focusing and defocusing effects. The scattering attenuation  $Q_S^{-1}(\omega)$  can be computed from,

$$\ln \left[ \frac{A(\omega)}{A_0(\omega)} \right] = \frac{\omega Q^{-1}}{2V} L. \quad (3)$$

This indicates that the logarithm of the spectral ratios is a linear function of source–receiver distances. We fit a straightline to  $\ln[A(\omega)/A_0(\omega)]$  and the slope of the line can be used to compute  $Q^{-1}(\omega)$ .

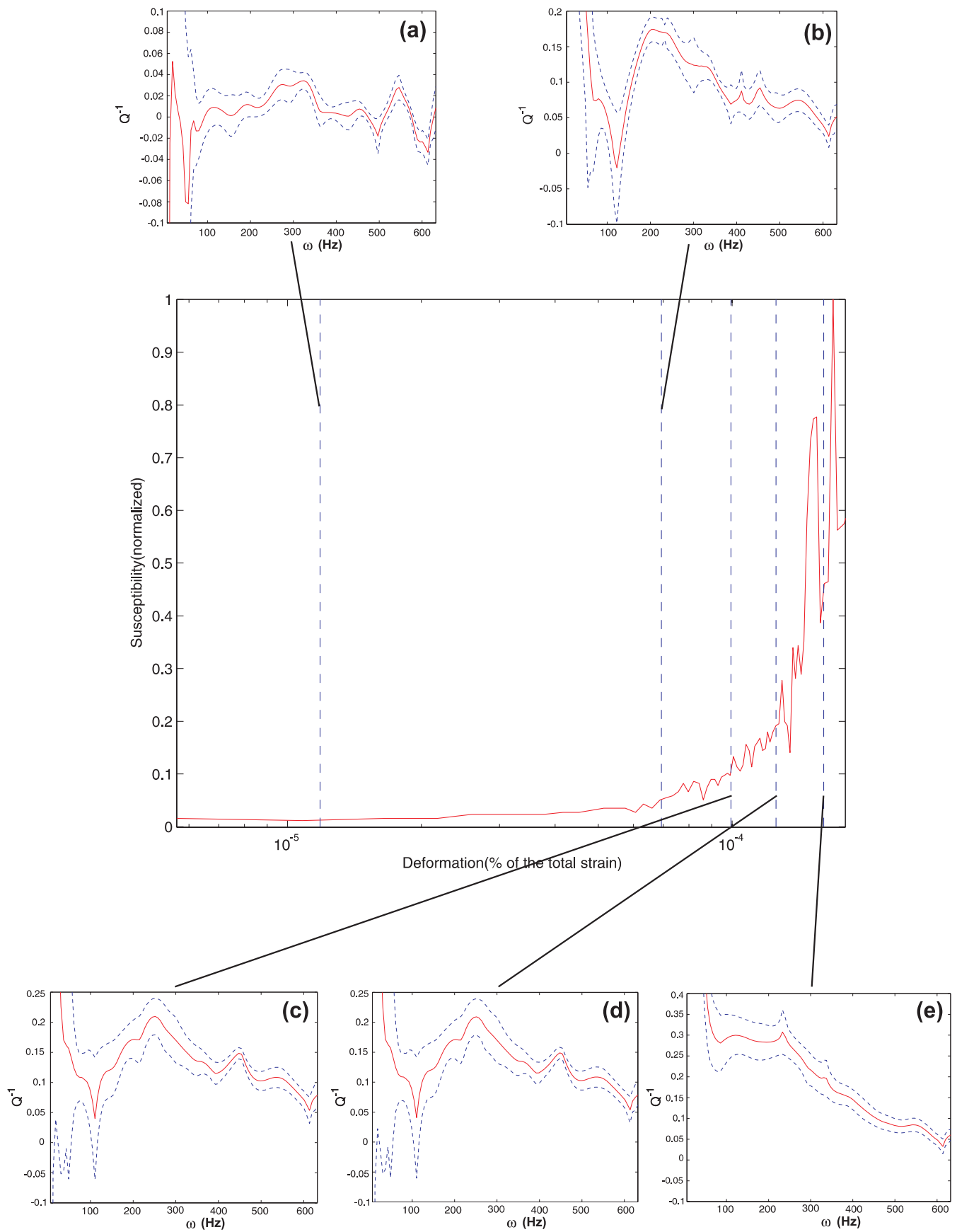
#### 4.2 Scattering attenuation as a function of susceptibility and deformation

We now present the quality factor  $Q^{-1}$  values for the frequency range (frequency in the range of 0–100 Hz) for the fracture patterns presented in Fig. 1. The results for very low- and very high-frequencies are less reliable due to low energy content in the source wavelet. Fig. 4 shows the normalized ‘susceptibility’ of the deformation field to small changes in stress for the states (a)–(e) of the fractured medium evolution (Narteau 2007). The susceptibility  $K$  is a good approximation of the correlation length of the system. If  $K = 1$ , the correlation length is infinite which corresponds to the percolation threshold. Deformation is presented as a percentage of total strain in the medium. In an evolving medium, strain will constantly grow as it evolves, so in this case deformation is representing a timescale of the evolution. The evolution of  $K$  is shown in Fig. 4 with dotted lines indicating the times when the fracture populations (a)–(e) shown in Fig. 1 occur. For each time we show the respective plot of the quality factor as a function of frequency. At each plot the straightlines represent the values of the quality factor, while the two dotted lines show the upper and lower limits of the error bars. Starting from state (a), the susceptibility has a very low value. At this stage there are only microscopic structures which are active cells and they are distributed throughout the medium, but there are no fractures. The quality factor has small fluctuations in its values but on average it has very low values. That is expected because the microscopic structures, compared to the wavelength, do not cause significant scattering. At stages (b)–(d), fractures of different length scale as well as microscopic structures begin to appear. Susceptibility rises exponentially from stage (b) to stage (d), because once the first fractures are created together with the growing procedure they undergo an interaction procedure which leads to larger fractures. In all stages the quality factor is much higher than in stage (a) because the size of the fractures is larger than or even comparable to the wavelength, which causes stronger scattering. At stage (b) we see a global maximum at  $\omega = 208$  ( $f = 33.1$  Hz) and two local maxima at  $\omega = 411$  ( $f = 65.4$  Hz) and  $\omega = 454$  ( $f = 72.3$  Hz). Those maxima may be directly linked to the characteristic scalelengths of the fractures. At stages (c) and (d), fractures have longer sizes and the quality factor is higher than stage (b). There are two maxima, a global one at  $\omega = 251$  ( $f = 40$  Hz) and a local one at  $\omega = 447$  ( $f = 71.2$  Hz), which implies that there are two dominant scales. At stage (e), we are one step before normalized susceptibility reaches one

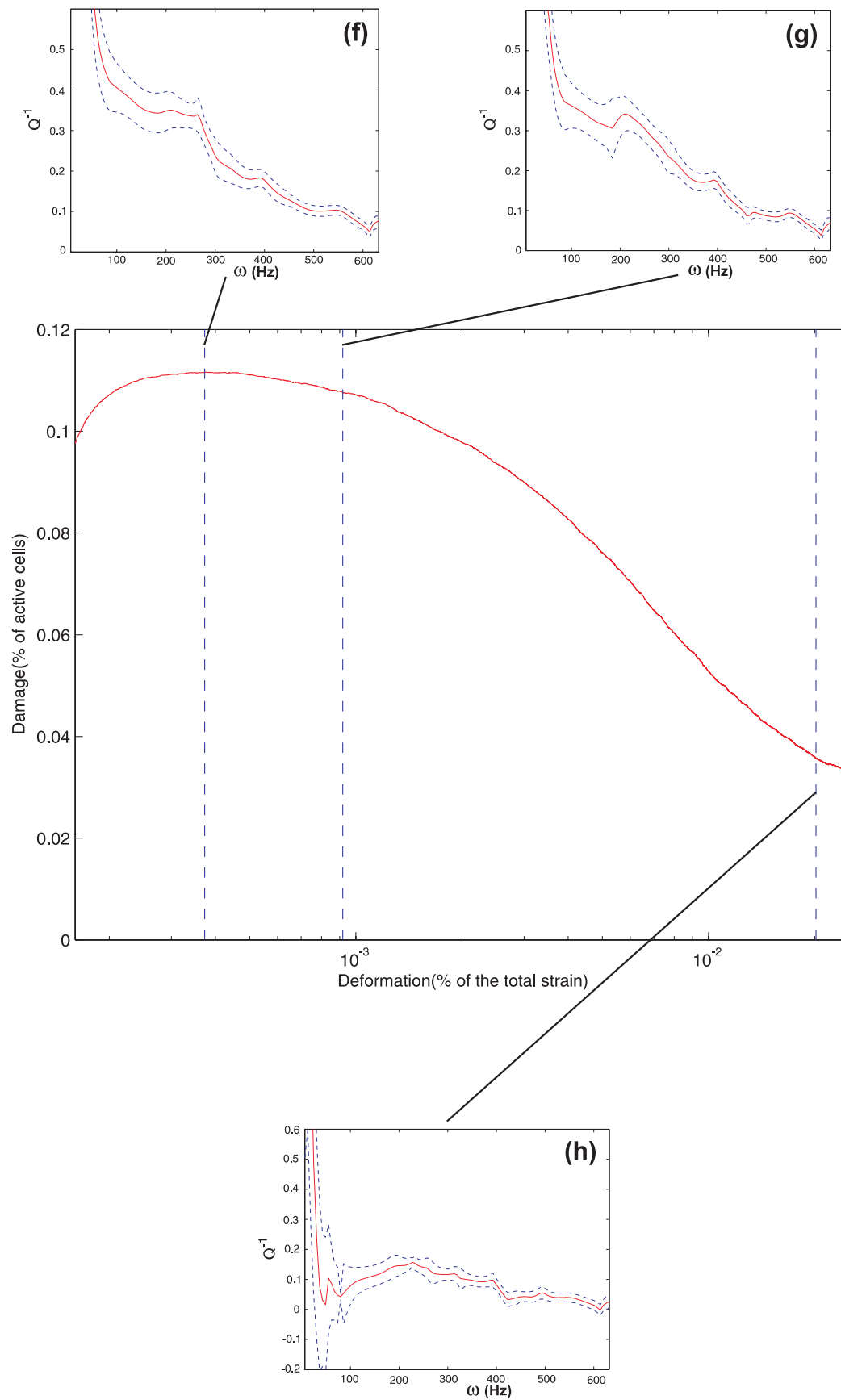
(the percolation threshold). Damage is still distributed via fractures and microscopic structures as in the previous stages. However at that stage there is no dominant scale. The quality factor in this case is much higher than the previous stages, because fracture density is higher. Nevertheless, the pattern of quality factor is very different from the previous stages. It has small fluctuations in the value, but generally we can see a straightline decreasing from 0.4 to 0.1 on linear–linear axes, with no clear maxima. That suggests that there is no characteristic scale in the system, consistent with the observations of Wu & Aki (1985) for the real Earth. This implies that the active tectonic areas that they examined were due to a critical stress state defined by the percolation threshold.

Fig. 5 shows the damage of the system as a function of deformation. The damage is defined as the ratio between the number of active cells and the number of stable cells as a percentage. For dilute damage, the damage equates to the crack density defined to be the number of cracks per unit area multiplied by the square of the scale (Hudson 1981). The ‘deformation’ here as in Fig. 4 is the timescale of the evolution. The dotted lines indicate the times when the fracture populations (f)–(h) shown in Fig. 1 occurred. Stage (f) has the highest damage, and after that the system moves towards localization and damage decreases at a constant rate at stages (g) and at stage (h) it reaches 1/5 of the value at stage (f). At stage (h) all the small scale damage disappears, so from that stage onwards there only large fractures and no microscopic cracks or small scale features exist. In all three stages we are still at the percolation threshold, so there is no characteristic scale. The quality factor  $Q^{-1}$  at stages (f) and (g) has almost the same pattern. The overall magnitude of attenuation is higher than stage (e) in both cases because fracture density is higher. It follows the same pattern as in stage (e) and declines at an almost constant rate with frequency apart from small fluctuations. At stage (g) there is a possible local maximum at  $\omega = 208$  ( $f = 33.1$  Hz), but it is not very clear. That may imply that after the percolation threshold the system is reorganized and a new characteristic length scale dominates. At stage (h), when the microscopic features disappear, that change on the properties of the medium is demonstrated clearly in the pattern of quality factor. At that stage, damage has a very low value, which means that the number of active cells is less than in the previous stages. As a result, scattering is less, as shown in the quality factor  $Q^{-1}$  that has values around 0.1 compared to average values between 0.3 and 0.4 in stages (f) and (g). It is almost constant with frequency with a small fluctuation in its values. The change in the pattern of quality factor may provide a potential means of identifying changes in the properties of heterogeneities.

Fig. 6 shows the normalized length of the fractures as a function of deformation. Again the deformation is proportional to the timescale of the evolution, and the dotted lines indicate the times when the fracture populations (i)–(l) shown in Fig. 1 occurs. At the final stages of the evolution of the system, there is no more growth of new fractures. However, existing fractures interact and form big fractures. This feature is demonstrated in Fig. 6, where we see that the normalized length rises sharply, although it has some fluctuations, until it reaches a maximum and it becomes constant at  $L = 1$  in the two final stages. At stage (i) the quality factor has a very similar variation to stage (h) with an almost constant value for all frequencies (although it slightly decreases at high frequencies). However, in this stage the local maximum that was not seen at stage (h) becomes visible here at  $\omega = 263$  ( $f = 41.9$  Hz). Seismic waves probably ‘recognize’ the characteristic scale. At stage (j) the first major fracture appears (Fig. 1j), which is a result of fracture interaction. Attenuation starts from a low value at small frequencies and it rises until it reaches a maximum



**Figure 4.** Normalized susceptibility as a function of deformation for stages (a)–(e) of the evolution of the fracture network. For each stage (a)–(e), we show the quality factor as a function of frequency.



**Figure 5.** Variation of the damage as a function of deformation for consecutive stages (f)–(h) of the evolution of the fracture network. The quality factor is also shown for all stages (f)–(h).

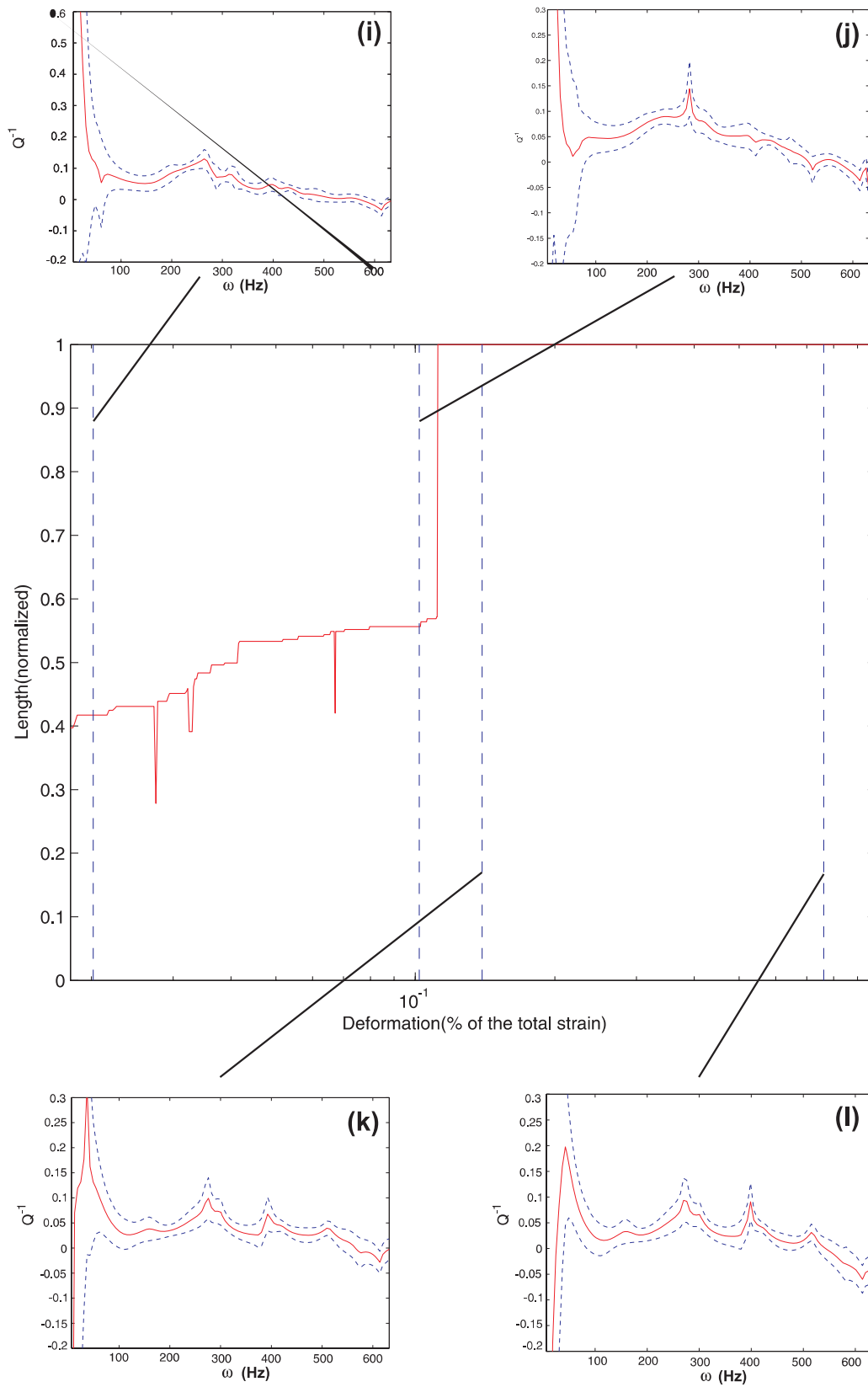


**Figure 6.** Normalized correlation length of the fractures as a function of deformation for stages (i)–(l), accompanied by the quality factor as a function of frequency for each stage.

at  $\omega = 282$  ( $f = 44.9$  Hz) and then drops monotonically. We expect that this maximum in quality factor is linked with the scale of major fractures. At stage (k) the system is almost at the end of its evolution. The major fracture is already formed and here the smaller secondary fractures that have almost the same size are generated. The quality factor shows almost the same pattern as in stage (j), but in this case there is a global maximum at  $\omega = 276$  ( $f = 43.9$  Hz), a local maximum at  $\omega = 392$  ( $f = 62.4$  Hz) and possibly another local maximum at  $\omega = 509$  ( $f = 81$  Hz) (Fig. 6k). So the global maximum is slightly shifted to a lower frequency compared with stage (j), which may indicate a small change in size, and we also have a clear local minimum. The two local minima may be related to the fact that at stage (i) the system has other heterogeneities that on average they have two distinct dominant scales. The final stage (l) when the system reaches stability has a similar variation in attenuation to state (k), with one global and two local maxima. However, the global maximum is also shifted to a slightly smaller frequency and the two local maxima are shifted to slightly higher frequencies (Fig. 6l). That can be interpreted as small changes in the dominant scale lengths.

### 4.3 Polynomial fitting to scattering attenuation

We fit a polynomial to the data with an order from 1 to 8. We use a statistical criterion and examine each one of the 12 states. The most commonly used statistical criteria for selecting a parsimonious model to describe the data are the Schwarz Information Criterion (SIC) proposed by Leonard & Hsu (1999, p. 8), Akaike's (1978) Information Criterion (AIC) and the Bayesian Information Criterion (BIC). When number of data is  $n > 46$ , computer simulations by Koehler & Murphree (1988) have shown that BIC is superior to other statistical criteria. In our case  $n = 103$ , and the BIC criterion is used,

$$\text{BIC} = L(y) - 0.5p \ln \left( \frac{n}{2\pi} \right), \quad (4)$$

where  $L(y)$  is the maximized logarithmic likelihood,  $n$  is the number of data points, and  $p$  is the number of unknown parameters in the model, that is, in our case the order of the polynomial we want to fit. This parameter ( $p$ ) is actually an extra penalty for the increase of the model complexity. The maximum logarithmic likelihood is given by,

$$L(y) = -0.5n \ln(S_R^2), \quad (5)$$

where  $S_R^2$  is the residual sum of squares and is given by,

$$S_R^2 = \sum_{i=1}^n [y_i - \gamma(x_i)]^2, \quad (6)$$

where  $y_i$  are the data points and  $\gamma(x_i)$  are the calculated values of the data points based on the polynomial fit. Fig. 7 shows the BIC criterion for the stages (a)–(l) of evolution for the various orders of polynomial. We can see that the order of polynomial with the highest BIC value is not consistent for all the stages. However, in most cases a polynomial of order 5 seems to give the optimal fit, so we decide to fit the data for all stages with a polynomial of order 5.

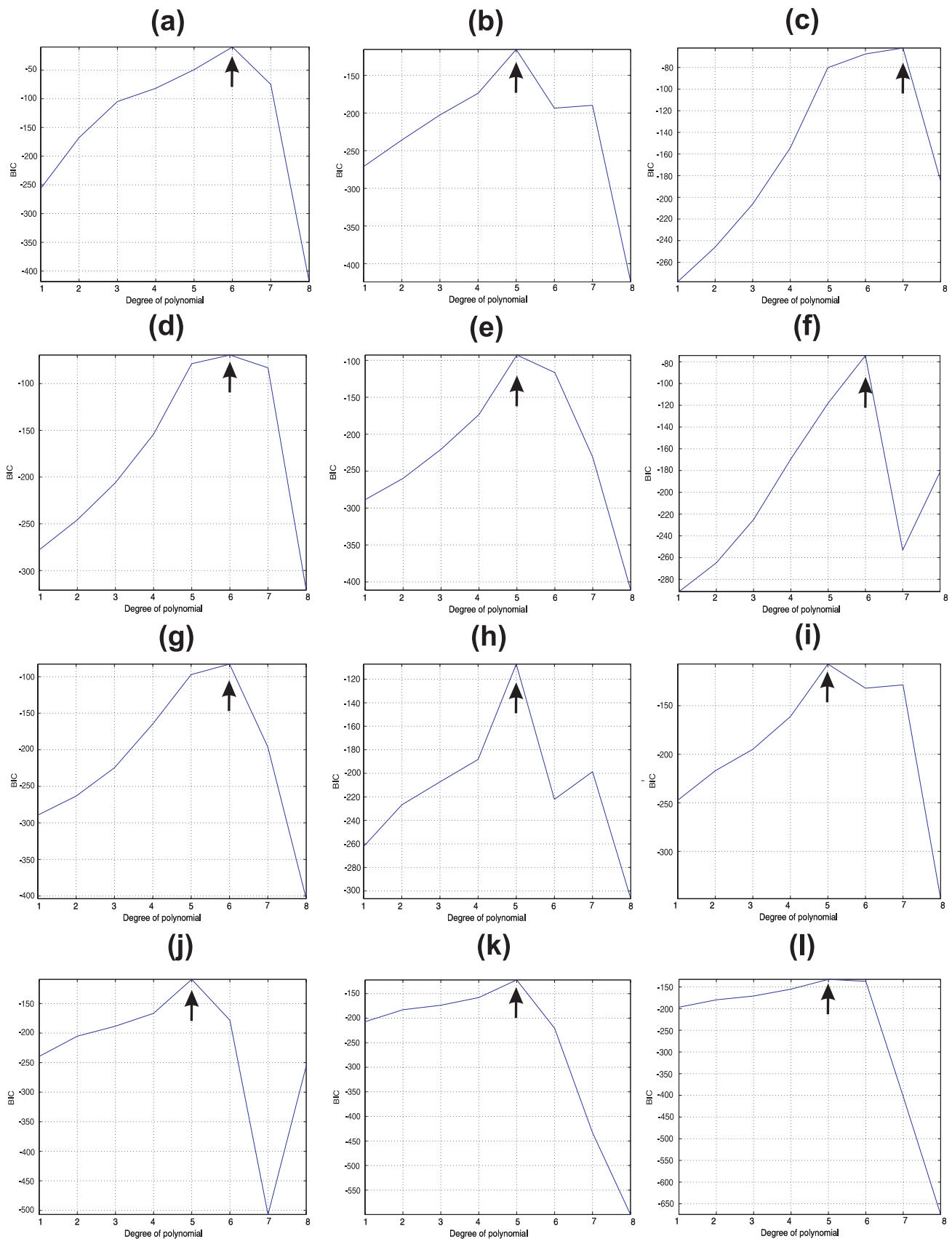
### 4.4 Directional dependence and $Q$ anisotropy

The scattering attenuation discussed in the previous section depends on fracture density and fracture scales. Another parameter affecting attenuation is the source–receiver orientation relative to the orientation of the fractures. This effect is generally known as

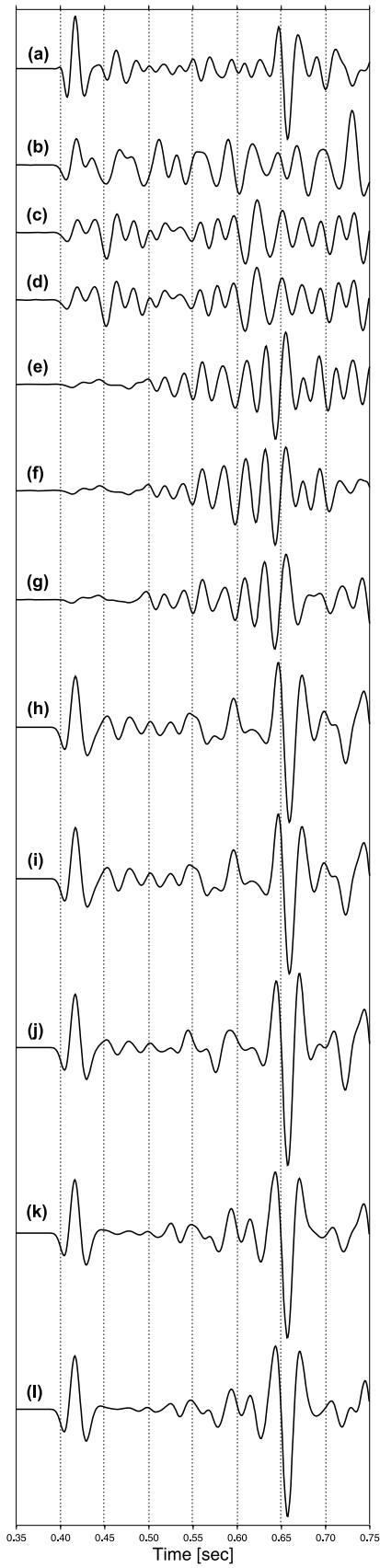
scattering-related attenuation anisotropy (Liu & Zhang 2001). Fig. 8 shows the synthetic vertical seismograms recorded at  $x = 700$  m and  $y = 300$  m, where the ray direction is almost parallel to the dominant orientation of the fractures. Waveforms (a)–(l) correspond to the states (a)–(l) in Fig. 1. In Fig. 8(a) we may identify both  $P$ - and  $S$ -wave arrivals, and scattered waves between 0.45 and 0.62 s. In Figs 10(b–d) the amplitudes of  $P$  waves gradually decrease and scattered (coda) wave energy becomes significant. That is exactly what we see in Figs 4(b–d). Figs 10(e–g) show strong attenuation of  $P$  waves, that is, there is a limited amount of energy in  $P$  waves. The energy is redistributed in the coda-waves that have much higher energy than in the previous cases. Also the coda-waves show a variety of frequency contents. Figs 10(h and i) show a change in the waveforms. Again there is high energy in  $P$  and  $S$  waves and some scattering that distributes energy in the coda-waves, although scattering is significantly lower than before. This is in agreement with the results shown in Figs 5(h) and 6(i). An interesting feature is that the amplitudes of  $S$  waves are larger than the amplitudes in Fig. 8(a), as a result of constructive interference. In contrast,  $P$  waves are less affected. The simple explanation is that when the ray direction is parallel to the dominant direction of fracturing,  $P$  waves are polarized in the propagation direction while  $S$  waves are polarized normal to the ray direction. Finally, Figs 10(j–l), show much less scattered energy in the coda waves and strong  $P$  and  $S$  waves.

Fig. 9 shows the vertical displacements recorded at  $x = 2250$  m and  $y = 720$  m, where the ray direction is almost normal to the dominant direction of fracturing. Waveforms (a)–(l) correspond to states (a)–(l) shown in Fig. 1. By comparing Figs 9 and 10, one clear observation is that the amplitudes of  $P$  waves in Fig. 9 are smaller than those in Fig. 8, while the amplitudes of  $S$  waves are larger in Fig. 9 than in Fig. 8. That is because in Fig. 9,  $P$  waves propagate normal to the fracture orientation while in Fig. 8 they travel along the fracture direction, therefore suffering more scattering in Fig. 9. The opposite happens with  $S$  wave as their direction of polarization is normal to  $P$  waves, and as a result  $S$  waves are less scattered. Note that the systematic azimuthal variations of scattered waves have been observed in field data by Minsley *et al.* (2004) and Willis *et al.* (2004), and the results from our work provides further confirmation to their claim that analysis of scattered waves may be used to characterize fractured hydrocarbon reservoirs.

We now summarize our results in Fig. 10. The circles represent states (a)–(l) and the  $x$ -axis is the deformation as in Figs 5–7. State (a) has the lowest attenuation, and we see a sharp increase until state (b) which is the initialization of growth. Attenuation continues to increase gradually at states (c) and (d), followed by a sharp increase in attenuation between (d) and (e), which continues between (e) and (f) where the maximum attenuation occurs. In Figs 10(f) and 11(f), the wave traces show the maximum attenuation, which coincides with the state of evolution where there are both a maximum fracture density and a maximum bandwidth of the different scales in the fracture length distribution (Fig. 10). Afterwards the localization of the deformation along major fractures occurs and thus at stages (h) and (i) fracture density decreases. As a result, attenuation decreases significantly. Finally, there is a dominant major fracture with some intermediate sized fractures, which makes reflection dominate and scattering attenuation even lower. This highlights the difference between coherent reflection from a linear interface, and the more random or incoherent nature of multiple scattering from a population of less organized fractures. We can see the resulting continuous decreases in  $Q^{-1}$  in Fig. 10, until it reaches the minimum at state (l).



**Figure 7.** Plot of the BIC criterion, as defined in eq. (4), as a function of the order of the polynomial. The order of the polynomial that gives the best fit is the one with the highest value of BIC. An arrow points to the order of the polynomial that gives the best fit for all states (a)–(l). For most states the best fit is given by a polynomial of order 5.



**Figure 8.** Synthetic seismograms recorded at a receiver situated at  $x = 700$  m and  $y = 300$  m for all states (a)–(l) shown in Fig. 1. The source–receiver direction is approximately parallel to the dominant direction of fractures.

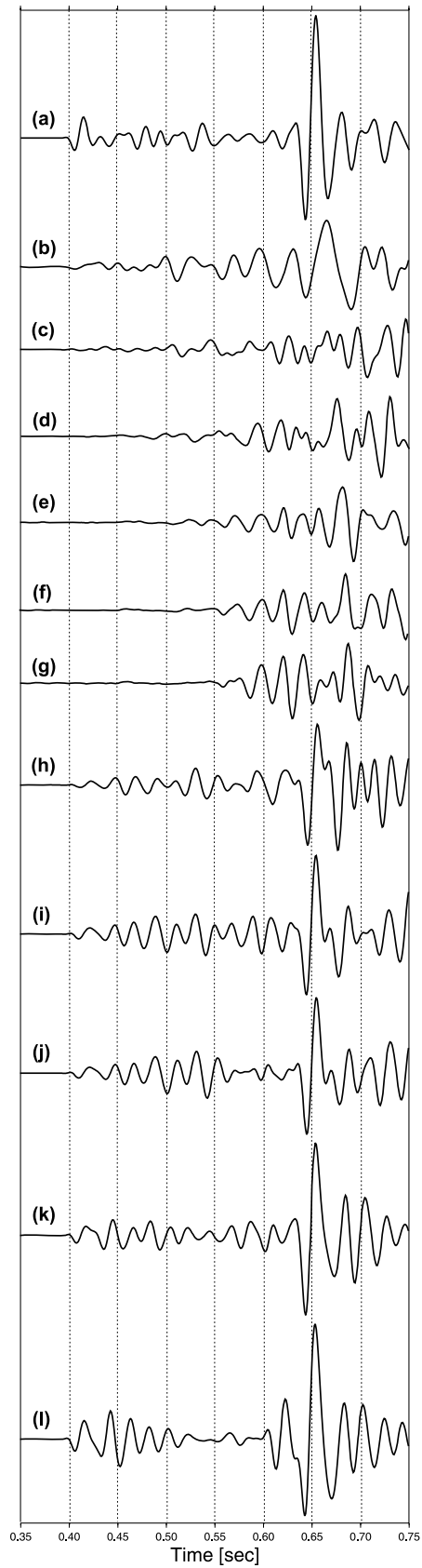


**Figure 9.** Synthetic seismograms recorded at a receiver situated at  $x = 2250$  m and  $y = 720$  m for all states (a)–(l) shown in Fig. 1. The source–receiver direction is approximately perpendicular to the dominant direction of fractures.

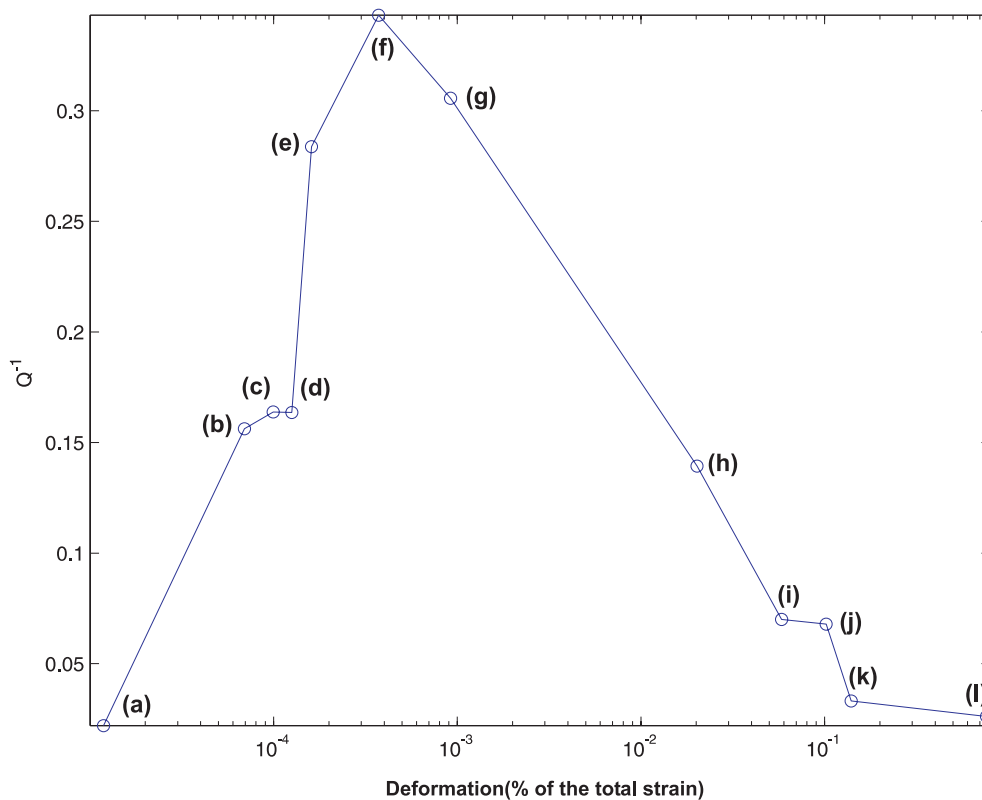


**Figure 10.** Scattering attenuation at the dominant source frequency ( $f = 30$  Hz), for all stages (a)–(l). The circles represent the values at the consecutive stages of evolution.

## 5 CONCLUDING REMARKS

We have conducted a systematic study of multiple scattering in a stochastic–deterministic model of an evolving fractured network generated using a multiscale cellular automaton model. Several models of fracture networks at consecutive stages of the evolution are presented, along with the variation in susceptibility, damage, and dominant length of fractures. We generate synthetic seismograms for each model representing different stages of the evolution and computed multiple scattering attenuation for each state as a function of frequency in order to fit polynomials to measured attenuation. A statistical method based on the Bayesian Information Criterion is used to select the polynomials.

Our results confirm that scattering attenuation is strongly frequency dependent, and the way attenuation varies with frequency depends on frequency ranges and particularly fracture scale distributions. The relationship between scattering attenuation and frequency has a complex variation at different stages of fracture evolution. One parameter that directly affects scattering attenuation is fracture density. We demonstrate that there is a proportional relationship between scattering attenuation and fracture density, so attenuation becomes stronger as fracture density increases, as expected.

Another parameter that greatly influences attenuation is the scale of fractures. Although seismic waves suffer scattering at fractures of sizes comparable to wavelength, smaller or larger fractures suffer less scattering. Maximum scattering attenuation correspond to the stages that fractures have a variety of scales (i.e. the percolation threshold). The sensitivity of scattering attenuation can also be used to indicate dominant scales of fractures by identifying wavelengths where maximum scattering occurs, as seen in the results of the final

stages of fracture evolution. Finally, we also highlight the fact that scattering attenuation varies with azimuth, and the highest values correspond to the propagation direction perpendicular to fractures and the lowest values to parallel to the fractures.

The results from this study give a clear indication that there is a potential to use scattering attenuation to characterize fracture properties and identify dominant scale lengths of fractures. Although in real data it is not easy to discriminate between scattering attenuation and intrinsic attenuation, attenuation measurements, in particular the measurement of differential (or relative) attenuation as promoted by Maultzsch *et al.* (2007), may be potentially used towards an improved characterization of fractured reservoirs in terms of spatial and size distributions of fractures. Recent advance in coda-wave interferometry provides an alternative way to characterize multiple scattering of seismic waves (Snieder *et al.* 2002; Gret *et al.* 2006), in particular small variations in physical properties (fluids, velocity and density) can be quantified from scattering waves (a numerical study was presented in our previous paper by Vlastos *et al.* 2006, and field data was given by Gret *et al.* 2006).

## ACKNOWLEDGMENT

We thank Mark Chapman, John H. Queen, Nick Barton, Michael Worthington, Zhongjie Zhang and Dinghui Yang for discussions on various occasions during this research. We also thank the GJI editors: Russ Evans, Cindy Ebinger, John A. Hudson and four anonymous reviewers, for their detailed comments which significantly improve the readability of this paper (this paper was originally submitted to GJI in 2003). The research was supported by the sponsors of the Edinburgh Anisotropy Project (EAP) and this paper is published

with the approval of the Executive Director of the British Geological Survey (BGS, NERC). Clement Narteau was supported through a Marie Curie fellowship (No HPMFT-2000-00669) from the European Community. One of the authors (EL) acknowledges the support of the National Natural Science Foundation of China NSFC for his visit to the China University of Mining and Technology (NSFC 40574058) while he was employed by BGS.

## REFERENCES

- Akaike, H., 1978. Bayesian analysis of the minimum AIC procedure, *Ann. Instit. Stat. Math.*, **30A**, 9–14.
- Aki, K. & Richards, P.G., 2002. *Quantitative Seismology*, 2nd edn, University Science Books, Sausalito, California.
- Barton, N., 2007. *Rock quality, Seismic Velocity, Attenuation and Anisotropy*, Taylor and Francis, London.
- Barton, N. & Bandis, S., 1980. Some effects of scale on the shear strength of joints, *Int. J. Rock Mech. & Min. Sci. & Geomech. Abstr.*, **17**, 69–73.
- Bonnet, E., Bour, O., Odling, N.E., Davy, P., Main, I., Cowie, P. & Berkowitz, P., 2001. Scaling of fracture systems in geological media, *Rev. Geophys.*, **39**, 347–383.
- Chapman, M., 2003. Frequency dependent anisotropy due to meso-scale fractures in the presence of equant porosity, *Geophys. Prospect.*, **51**, 369–379.
- Coates, R.T. & Schoenberg, M., 1995. Finite-difference modelling of faults and fractures, *Geophysics*, **60**, 1514–1526.
- Crampin, S., 1978. Seismic wave propagation through a cracked solid: polarization as a possible dilatancy diagnostic, *Geophys. J. R. Astr. Soc.*, **53**, 467–496.
- Crampin, S., 1984. Effective anisotropic elastic constants for wave propagation through cracked solids, *Geophys. J. R. Astr. Soc.*, **76**, 135–145.
- Gret, A., Snieder, R. & Ozbay, U., 2006. Monitoring in situ stress changes in a mining environment with coda wave interferometry, *Geophys. J. Int.*, **165**, 485–500.
- Hudson, J.A., 1981. Wave speeds and attenuation of elastic waves in material containing cracks, *Geophys. J. R. Astr. Soc.*, **64**, 133–150.
- Hudson, J.A., 1986. A higher order approximation to the wave propagation constants for a cracked solid, *Geophys. J. R. Astr. Soc.*, **87**, 265–274.
- Hudson, J.A., Liu, E. & Crampin, S., 1996. Transmission properties of a plane fault, *Geophys. J. Int.*, **125**, 559–566.
- Hudson, J.A., Liu, E. & Crampin, S., 1997. The mean transmission properties of a fault with imperfect facial contact, *Geophys. J. Int.*, **129**, 720–726.
- Jin, A. & Aki, K., 1986. Temporal change in coda  $Q$  before the Tangshan earthquake of 1976 and the Haicheng earthquake of 1975, *J. geophys. Res.*, **91**, 665–673.
- Koehler, A.B. & Murphree, E.S., 1988. A comparison of Akaike and Schwarz criteria for selecting model order, *Appl. Stats.*, **37**, 187–195.
- Leary, P.C., 1995. The cause of frequency-dependent seismic absorption in crystal rock, *Geophys. J. Int.*, **122**, 143–151.
- Leonard, T. & Hsu, J.S.J., 1999. *Bayesian Methods*, Cambridge University Press, New York.
- Lerche, I., 1985. Multiple scattering of seismic waves in fractured media: cross-correlation as a probe of fracture intensity, *Pure Appl. Geophys.*, **123**, 503–542.
- Lerche, I. & Petroy, D., 1986. Multiple scattering of seismic waves in fractured media: velocity and effective attenuation of the coherent components of  $P$ -waves and  $S$ -waves, *Pure Appl. Geophys.*, **124**, 975–1019.
- Liu, E., 2005. Effects of fracture aperture and roughness on mechanical and hydraulic properties of rocks: implication of seismic fracture characterization, *J. geophys. Eng.*, **2**, 38–47.
- Liu, E. & Zhang, Z.J., 2001. Numerical study of elastic wave scattering by distributed cracks or cavities using the boundary integral method, *J. Comp. Acoust.*, **9**, 1039–1054.
- Liu, E., Hudson, J.A., Crampin, S., Rizer, W.D. & Queen, J.H., 1995. Seismic properties of a general fracture, in *Mech. Jointed and Faulted Rock*, pp. 659–664, ed. H.P. Rossmanith, A.A. Balkema Publishers, Rotterdam.
- Liu, E., Hudson, J. & Pointer, T., 2000. Equivalent medium representation of fractured rock, *J. geophys. Res.*, **105**, 2981–3000.
- Liu, E., Chapman, M., Zhang, Z.J. & Queen, J.H., 2006. Frequency-dependent anisotropy: effects of multi-fracture sets on shear-wave polarizations, *Wave Motion*, **44**, 44–57.
- Liu, K., Zhang, Z.J., Hu, J. & Teng, J., 2001. Frequency-band dependence of  $S$ -wave splitting in China mainland and its implications, *Science in China (Series D)*, **47**, 569–665.
- Lubbe, R. & Worthington, M.H., 2006. A field investigation of fracture compliance, *Geophys. Prospect.*, **54**, 319–331.
- Main, I.G., Peacock, S. & Meredith, P.G., 1990. Scattering attenuation and the fractal geometry of fracture systems, *Pure Appl. Geophys.*, **133**, 283–304.
- Minsley, B., Willis, M., Krasovec, M., Burns, D. & Toksoz, N., 2004. Investigation of a fractured reservoir using  $P$ -wave AVOA analysis: a case study of Emilio Field with support from synthetic examples, *74th Ann. Internat. Mtg., Soc. of Expl. Geophys.*, 248–251.
- Maultzsch, S., Chapman, M., Liu, E. & Li, X.Y., 2007. Modelling and analysis of attenuation anisotropy in multi-azimuthal VSP data from the Clair field, *Geophys. Prospect.*, **55**, 627–642.
- Narteau, C., 2007. Formation and evolution of a population of strike-slip faults in a multiscale cellular automaton model, *Geophys. J. Int.*, **168**, 723–744.
- Peacock, S. & Hudson, J.A., 1990. Seismic velocities of rocks with distributions of small cracks, *Geophys. J. Int.*, **102**, 472–484.
- Pointer, T., Liu, E. & Hudson, J.A., 2000. Seismic wave propagation in cracked porous media, *Geophys. J. Int.*, **142**, 199–231.
- Pyrak-Nolte, L.J., Myer, L.R. & Cook, N.G.W., 1990a. Transmission of seismic waves across single fractures, *J. geophys. Res.*, **95**, 8617–8638.
- Pyrak-Nolte, L.J. & Nolte, D.D., 1992. Frequency dependence of fracture stiffness, *Geophys. Res. Lett.*, **19**, 325–328.
- Pyrak-Nolte, L.J., Myer, L.R. & Cook, N.G.W., 1990b. Anisotropy in seismic velocities and amplitudes from multiple parallel fractures, *J. geophys. Res.*, **95**, 11, 345–11, 358.
- Schoenberg, M., 1980. Elastic wave behaviour across linear slip interfaces, *J. Acoust. Soc. Am.*, **68**, 1516–1521.
- Snieder, R., Gret, A. & Douma, H., 2002. Coda wave interferometry for estimating nonlinear behaviour in seismic velocities, *Science*, **295**(22), 2253–2255.
- Sornette, D., Miltenberger, P. & Vanneste, C., 1994. Statistical physics of fault patterns self-organized by repeated earthquakes, *Pure Appl. Geophys.*, **142**, 491–527.
- Vlastos, S., Liu, E., Main, I.G. & Li, X.-Y., 2003. Numerical simulation of wave propagation in media with discrete distributions of fractures: effects of fracture sizes and spatial distributions, *Geophys. J. Int.*, **152**, 649–668.
- Vlastos, S., Liu, E., Main, I.G., Schoenberg, M., Narteau, C., Li, X.-Y. & Maillot, B., 2006. Dual simulations of fluid flow and seismic wave propagation in a fractured network: effects of pore pressure on seismic signature, *Geophys. J. Int.*, **166**, 825–838.
- Willis, M., Rao, R., Burns, D., Byun, J. & Vetri, L., 2004. Spatial orientation and distribution of reservoir fractures from scattered seismic energy, *74th Ann. Internat. Mtg., Soc. of Expl. Geophys.*, 1535–1538.
- Wu, R., 1982. Attenuation of short period seismic waves due to scattering, *Geophys. Res. Lett.*, **9**, 9–12.
- Wu, R. & Aki, K., 1985. The fractal nature of the inhomogeneities in the lithosphere evidenced from seismic wave scattering, *Pure Appl. Geophys.*, **123**, 805–818.
- Yang, D.H., Shen, Y. & Liu, E., 2007. Wave propagation and the frequency domain Green's functions in viscoelastic Biot/squirt (BISQ) media, *Int. J. Solids & Struct.*, **44**, 4784–4794.
- Yang, D.H. & Zhang, Z.J., 2002. Poroelastic wave equation including the Biot/Squirt mechanism and the solid/fluid coupling anisotropy, *Wave Motion*, **35**, 223–245.
- Yue, J.H., Liu, E. & Liu, S.C., 2007. Effects of pore fluids on the interfacial and fracture compliances, *J. Seism. Explor.*, **15**, 367–385.

## APPENDIX A: EVOLUTION OF FRACTURES

In the initial stages of the nucleation phase there are isolated active fracture segments (Fig. 1a). Since fracture interaction is negligible, these fracture nuclei have a random homogeneous spatial distribution, and their number increases at a constant rate. The strain rates remain virtually uniform and only small fluctuations can be distinguished in the neighbourhood of the fracture nucleus. Nevertheless, they favour the accumulation and the concentration of the strain rates on the fracture segment and at the fracture tips while they impede it on each side of the fault.

While the nucleation process continues, the strain rates are primarily concentrated on the process zones of the fracture nucleus. In these process zones, the intensity of the microfracturing process increases and fractures may grow (Fig. 1b). Given the orientation of the external tectonic loading, the new fractures have an orientation close to the main direction (Fig. 1c). During the growth phase, the fracture tips move faster as the fracture becomes larger because the redistribution mechanism in the neighbourhood of active fractures ensures a non-linear feedback processes in the fracture growth mechanism.

When the nucleation process is almost nonexistent and as the growth process continues (Fig. 1d), the ratio between the length of the fractures and their distance increases and the fractures begin to interact. There are three types of interactions: (i) Overlap of process zones when two fractures propagate towards the same zone, (ii) overlapping shadow zones when two parallel fractures propagate

simultaneously and (iii) overlap of shadow and process zones in any step-like discontinuity. These interactions can efficiently modify the geometry of the fracture network and new fracture patterns emerge (Fig. 1e). Fractures may coalesce to form curved patterns while other fractures may produce en-echelon patterns. As a result of the growth phase and of the first stages of the interaction phase, the density of active fracture segment is high and the fracture population is characterized by active fractures of all dimensions (Fig. 1f).

From the hierarchy established at the end of these preliminary phases of fracture growth (Fig. 1g), the fracture population evolves towards a more stable configuration based on the coexistence of major faults. During this concentration phase, major fractures increase their strain rates by removing the strain rates from minor fractures. Thus the active fracture population becomes less compact (Fig. 1h) and small fractures become inactive. Along major fractures of different lengths, the connected active segments tend to form a smoother fracture trace. Branching and step-over disappear but bends between regular segments may persist. Hence, the strain rates are almost uniform but may vary according to the alignment of the fracture segments with respect to the dominate direction and remaining structural irregularities. Fractures may continue to grow if major fractures positively interact with each other (Fig. 1i). Finally, major fractures may connect with each other (Fig. 1j), and a unique fracture cutting the entire system may appear (Fig. 1k). This fracture localizes all the deformation and neighbouring active fractures disappear (Fig. 1l). This configuration of faulting is stable over a long timescale and may be described as the final stage of the localization process of the deformation.